Influence of fast ice on future ice shelf melting in the Totten Glacier area, East Antarctica

Guillian Van Achter[1], Thierry Fichefet[1], Hugues Goosse[1], and Eduardo Moreno-Chamarro[2]

[1]Earth and Life Institute, Georges Lemaitre Centre for Earth and Climate Research, UCLouvain, Louvain-la-Neuve, Belgium.
[2]Barcelona Supercomputing Center (BSC), Barcelona, 08034, Spain.

Correspondence: Guillian Van Achter (guillian.vanachter@uclouvain.be)

Abstract. The Totten Glacier in East Antarctica is of major climatic interest because of the large fluctuations of its grounding line and potential vulnerability to climate change. Here, we use a series of high-resolution, regional NEMO-LIM-based experiments, which include an explicit treatment of ocean–ice shelf interactions as well as a representation of grounded icebergs and fast ice, to investigate the changes in ocean–ice interactions in the Totten Glacier area between the last decades (1995-2014) and the end of the 21st century (2081-2100) under SSP4-4.5 climate change conditions. By the end of the 21st century, the wide areas of multiyear fast ice simulated in the recent past are replaced by small patches of first year fast ice along the coast, which decreases the total summer sea ice extent. The Antarctic Slope Current is accelerated by more than 90% and the Totten ice shelf melt rate is increased by 41% due to enhanced warm water intrusions into its cavity. The representation of fast ice dampens the ice shelf melt rate increase, as the Totten ice shelf melt rate increase reaches 58% when fast ice is not taken into account. The Moscow University ice shelf melt rate increase is even more impacted by the representation of fast ice, with a 1% melt rate increase with fast ice, compared to a 38% increase without a fast ice representation. This highlights the importance of including representation of fast ice to simulate realistic ice shelf melt rate increase in East Antarctica under warming conditions.

1 Introduction

The Totten Glacier area, located on the Sabrina Coast in East Antarctica, underwent significant grounding-line fluctuations during the recent past. Driven by changes in the ocean (Aitken et al., 2016), these fluctuations are making the region potentially vulnerable to rapid ice sheet collapse (Roberts et al., 2011). There has been some indication of ice shelf thinning during the last decade (Khazendar et al., 2013), although it remains unclear whether this represents a long-term trend (Paolo et al., 2015). Furthermore, the Totten catchment, located in the Aurora Subglacial Basin of East Antarctica, contains 3.5-m sea level rise equivalent and is one of the few sectors of East Antarctica where changes in ice dynamics have been observed recently (Greenbaum et al., 2015). Understanding how changes in the ocean–ice interactions are interfering with the basal melt of the Antarctic ice shelves and how they will evolve in the future is crucial for projections of future sea level rise.

A key element of the ocean–ice interactions in the Totten Glacier area is the fast ice (Van Achter et al., 2022), defined as stationary sea ice which forms and remains attached to the shore or between grounded icebergs (WMO, 1970; Massom et al.,

25 2001; Fraser et al., 2012). Numerous observations show the presence of multiyear fast ice in front of both the Totten and Moscow University ice shelves (Fraser et al., 2012, 2020). Van Achter et al. (2022) have clearly demonstrated with a numerical model (over the years 2001-2010) that the presence of fast ice in the Totten Glacier region impacts both the location of coastal polynyas and the ocean mixed layer depth along the coast, in addition to favouring the intrusion of modified Circumpolar Deep Water (mCDW) into the ice shelf cavities, with an enhanced or reduced ice shelf melting depending on the location. The loss

30 of buttressing from the break-up of seasonal fast ice increases the seasonality of the Totten ice shelf (TIS) basal melt rate close to the ice front (Greene et al., 2018).

Large density, temperature, salinity and sea level gradients are found across the Antarctic Slope Front (ASF; Whitworth et al., 1985; Jacobs, 1991), which separates the continental shelf from the open Southern Ocean. A strong pressure gradient is observed across the ASF, mainly caused by the strong easterly winds that drive a sea surface height gradient via Ekman drift

35 (Mathiot et al., 2011), as well as a density gradient, which results from the differences in temperature and salinity of the water masses across the ASF. Additionally, the ASF manifests itself through strong isopycnal doming towards the continental shelf. These lateral gradients across the ASF contribute to establishing the geostrophically balanced, vertically sheared along-slope flows of the Antarctic Slope Current (ASC; Jacobs, 1991; Thompson et al., 2018). The ocean dynamics associated with the ASF and ASC govern along- and across-slope heat transport (Stewart et al., 2018), and act as a barrier to mixing between shelf

40 and open-ocean waters (Thompson et al., 2018). Shifts in position of the ASF, or changes in the range of densities of waters that occupy the continental shelf, will therefore strongly influence the heat budget of the continental shelf (Thompson et al., 2018). Moorman et al. (2020) suggested that increasing glacial meltwater fluxes strengthens the lateral density gradient associated with the ASF, which reduces cross-slope water exchanges and isolates shelf waters from warm mCDW. Naughten et al. (2018) also found an intensified density gradient across the continental slope which reinforces the Antarctic Coastal Current. In the

45 Totten Glacier region, the ASC modulates the heat intrusion towards the Totten Glacier (Nakayama et al., 2021).

As a consequence, understanding how the ASC will evolve in this region under future climate conditions is key to gain insights on changes in heat intrusion across the continental shelf break. The future changes in ice shelf melt rate under different Representative Concentration Pathway (RCP) scenarios have been studied with both global and regional models (Hellmer et al., 2012; Timmermann and Goeller, 2017). In the Totten Glacier area, Pelle et al. (2021) found that, by the end of the 21st century,

50 the ASC might weaken by 37% compared to its present-day state and the Totten ice shelf melt rate might increase by 56% following a high emission scenario. Those models include representations of ocean–ice shelf interactions, but none of them has an prognostic representation of the fast ice.

The goal of this study is twofold. Firstly, we want to evaluate how the ocean–ice shelf interactions in the Totten Glacier region will change in a warming climate, with a particular focus on the ASC changes and their origin. Secondly, we aim at

55 assessing how an explicit fast ice representation included in a model affects the simulation of the ice shelf melt rate evolution between the last decades and the end of the 21st century. In order to answer these questions, we designed four simulations with a high-resolution, regional configuration of the NEMO3.6-LIM3 model, two of them being forced with anomalies derived from a simulation with the global climate model EC-Earth3 driven by the SSP4-4.5 scenario (Shared Socioeconomic Pathways; Döscher et al., 2021).

60 This manuscript is organised as follows. The model, regional configuration and experimental design are described in Section 2. In Section 3, we analyse the changes in sea ice and ocean characteristics and ice shelf melt rate between the last decades and the end of the 21st century simulated by the model. The sensitivity of the ice shelf melt rate to the representation of fast ice is then addressed in Section 4. Conclusions are finally given in Section 5.

2 The model, forcing and experimental design

2.1 Ocean–sea ice model

65 We make use of NEMO 3.6 (Nucleus for European Modelling of the Ocean; Madec, 2008) that includes the ocean model OPA (océan parallélisé) coupled with the Louvain-la-Neuve sea ice model (LIM3; Vancoppenolle et al., 2009; Rousset et al., 2015). This combination is hereafter referred to as NEMO-LIM. OPA is a state-of-the-art, finite-difference ocean model based on primitive equations. Our setting includes a polynomial approximation of the seawater equation of state (TEOS-10, IOC, 2010) optimized for a Boussinesq fluid (Roquet et al., 2014). Vertical turbulent mixing is rendered through a Turbulent Kinetic Energy (TKE) scheme (Bougeault and Lacarrere, 1989; Gaspar et al., 1990; Madec et al., 1998). The enhanced vertical diffusion mixing coefficient utilised in this scheme is fixed to 20 m^2/s. LIM3 uses a five-category subgrid-scale distribution of sea ice thickness (Bitz et al., 2001). The drag coefficient is set to 7.1×10^{-3} at the sea ice–ocean interface and 2×10^{-3} at the sea ice–atmosphere one (Massonnet et al., 2014). Ice shelf cavities with explicit ocean—ice shelf interactions are represented by the ice shelf module implemented in NEMO by Mathiot et al. (2017), using the three-equation formulation from Jenkins (1991). Transfer coefficients for heat (γ_T) and salt (γ_S) between the ocean and ice shelves are velocity dependent (Dansereau et al., 2014): $\gamma_{T,S} = \Gamma_{T,S} \times u_*$. The friction velocity is given by $u_* = C_d \times \sqrt{u_{TML}^2}$ and constant values of Γ_T and Γ_S taken from Jourdain et al. (2017) are employed ($\Gamma_T = 2.21 \times 10^{-2}$ and $\Gamma_S = 6.19 \times 10^{-4}$ for temperature and salinity, respectively). C_d is the top drag coefficient, set to 14×10^{-3}, and u_{TML} is the ocean velocity in the top mixed layer, which is either the top 30 m of the water column or the top model layer (if thicker than 30 m) (Losch, 2008).

2.2 The Totten24 model configuration

Here, we use a regional configuration of NEMO-LIM, referred to as Totten24, which is described in detail in Van Achter et al. (2022). The horizontal grid is a 1/24°refinement (less than 2 km grid spacing) of the eORCA1 tripolar grid, centered on the continental shelf in front of the TIS, East Antarctica, and covering an area between 108-129° E and 63-68° S (Fig. 1). The NEMO and LIM time steps are 150 s and 900 s, respectively. The vertical discretisation has 75 levels, with level thickness increasing with depth and partial cells used for better representing bedrock and ice shelf bases (Adcroft et al., 1997). The ocean layer directly underneath the ice shelf base varies between 30 m near the cavity front and 80 m in the center of the cavity. The bathymetry and ice shelf draft datasets are derived from the NASA Making Earth System Data Records for Use in Research

90 Environments (MEaSUREs) program, which contains a bathymetry map of Antarctica based on mass conservation, streamline
diffusion and other methods (Morlighem et al., 2020).

The ocean lateral boundary conditions and initial conditions are taken from a 1979-2014 simulation with an eORCA025
(1/4°, 75 levels) peri-Antarctic NEMO-LIM configuration (Pelletier et al., 2022) (hereafter referred to as PARASO). Because
of a negative salinity bias in the PARASO simulation, a salinity correction of 0.25 g/kg is uniformly added to the ocean lateral
95 boundary conditions and initial conditions. At the lateral boundaries, a flow relaxation scheme (Engedahl, 1995) is applied
to the three-dimensional ocean variables and two-dimensional sea ice variables. A Flather scheme (Flather, 1994) is used
for barotropic velocities and sea surface elevation. Furthermore, the sea surface elevation and barotropic velocities from the
FES2014 tide model (Carrère et al., 2012) are added to the boundary for the tide components K1, K2, M2, P1, O1, S2, 2N2,
Mm, M4, Mf, Mtm, MU2, N2, NU2, Q1, S1, L2, T2, as in Maraldi et al. (2013); Jourdain et al. (2019); Huot et al. (2021).
100 The surface fluxes of heat, freshwater and momentum are computed using the CORE bulk formulas (Large and Yeager, 2004),
with atmosphere input coming from the fifth generation ECMWF atmospheric reanalysis (ERA5, Hersbach et al., 2020). No
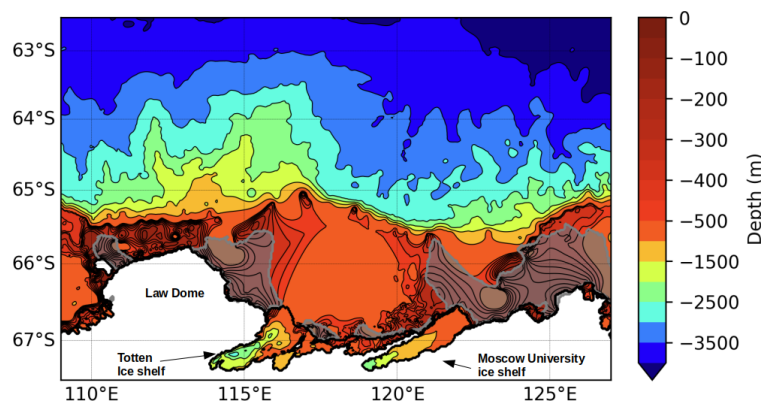surface salinity restoring is applied.

Figure 1. Model bathymetry and domain. The contour interval is 50 m up to 500 m depth and 500 m up to 4500 m depth. Ice shelf cavities
are surrounded by a thick black line. The 0.75 fast ice observed frequency from Fraser et al. (2020) is shown by the shaded gray areas.

2.3   Experimental design

Our experimental design consists of one reference simulation and a set of three sensitivity experiments. All simulations include
105 the tide constituents and the ocean–ice shelf interactions (i.e., open ice shelf cavities and interactive basal melt computation).
The reference simulation (REF) includes a representation of grounded icebergs and a sea ice tensile strength parameterisa-
tion. Both are needed to simulate adequately the fast ice formation (Van Achter et al., 2022). The grounded iceberg dataset
used is extracted from the remote sensed mosaic 'RAMP AMM-1 SAR Image Mosaic of Antarctica, Version2' (Jezek et al.,
2013) and covers the September-October months of 1997. The grounded icebergs are prescribed in the model by setting the
110 bathymetry value to zero at every iceberg location (see Van Achter et al. (2022)). The sea ice tensile strength parameterisation
was developed by Lemieux et al. (2016). The REF simulation covers the 1995 to 2014 period, with a 1993-1994 spin-up. A

similar simulation was conducted by Van Achter et al. (2022) and evaluated against observations. For the present study, the salinity bias identified in this study has been corrected (Fig. 2b), without altering the vertical profiles of temperature (Fig. 2a), and the top drag coefficient in the ice shelf cavities has been increased from 8×10^{-3} to 14×10^{-3} to reduce the ice shelf melt

115 rate bias. With these modifications, the simulated TIS melt rate (9.06 m/yr) is in better agreement with Rignot et al. (2013)'s estimate (10.47 ± 0.7 m/yr). This is also the case for the Moscow University ice shelf (MUIS), with a simulated melt rate of 5.95 m/yr, which is closer to the 4.7 ± 0.8 m/yr estimate of Rignot et al. (2013). Except for those changes in ice shelf melt rate and salinity profiles, results from this new REF simulation are very similar to those of the previous one in terms of sea ice distribution and ocean circulation.

120 The sensitivity experiments include the nFST, WARM and nFST_WARM simulations (Table 1). nFST is identical to REF but without fast ice representation i.e., no tensile strength parameterisation and no grounded icebergs representation. WARM and nFST_WARM have the same setup as REF and nFST, respectively, but cover the 2081-2100 period. In these simulations, the model is forced by climate anomalies derived from a climate change projection carried out with the global climate model EC-Earth3 under the SSP4-4.5 scenario (Döscher et al., 2021), within the 6th phase of the Coupled Model Intercomparison

125 Project (Eyring et al., 2016). Note that, in WARM, the grounded icebergs location are the same as in REF.
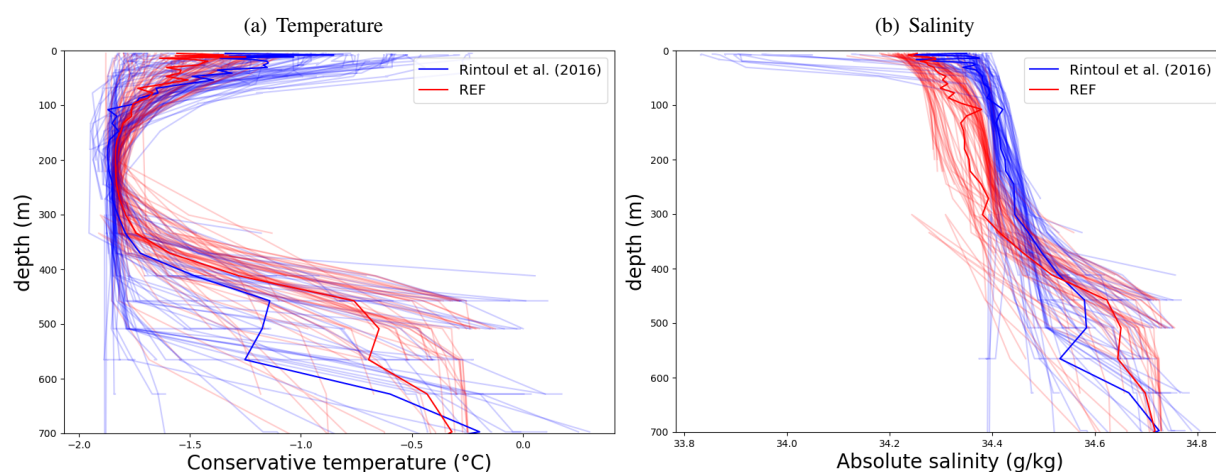

Figure 2. Vertical profiles of temperature (a) and salinity (b) on the continental shelf in front of the Totten ice shelf. Blue: CTD from Rintoul et al. (2016) (a1402). Red: as simulated in REF. Simulated profiles are taken at the same time and location as the CTD measurements.

Annual cycles of the EC-Earth3 climate anomalies are computed as the differences between 2081-2100 and 1995-2014, and are added to all the fields of the atmospheric and oceanic forcings used for the 1995-2014 period in REF and nFST (for the atmosphere: wind velocity, temperature, specific humidity, surface downward radiation and precipitation; for the ocean: current velocity, temperature, salinity, sea surface height, sea ice concentration, sea ice thickness and snow thickness). Figure 3 shows

130 the annual mean ocean temperature, salinity and zonal ocean velocity anomalies at the eastern boundary condition, and the mean near-surface (2 m) air temperature and atmospheric zonal wind (10 m) velocity anomalies. We show the ocean anomalies at the eastern lateral boundary condition as they are very similar to those at the western lateral boundary condition, and also

because the ocean eastern boundary condition is one of the drivers of the ocean dynamic over the continental shelf in regional modelling (Nakayama et al., 2021). The ocean temperature anomaly is positive everywhere, with values from 0 to $0.5°$ C over

135 the continental shelf and in the deep ocean, and from 1 to $1.5°$ C in the upper ocean outside of the shelf. The seawater salinity anomaly is mostly negative (down to -0.4 g/kg), with the lower values above the continental shelf. Oceanic zonal velocity anomalies at the eastern boundary are westward over the shelf and eastward off the shelf. The EC-Earth3 anomaly applied at the zonal wind component is mostly eastward over the ocean, increasingly towards the north. Westward winds anomaly also occur, but only over a small part of the shelf and over the continent. The surface air temperature anomaly is positive everywhere

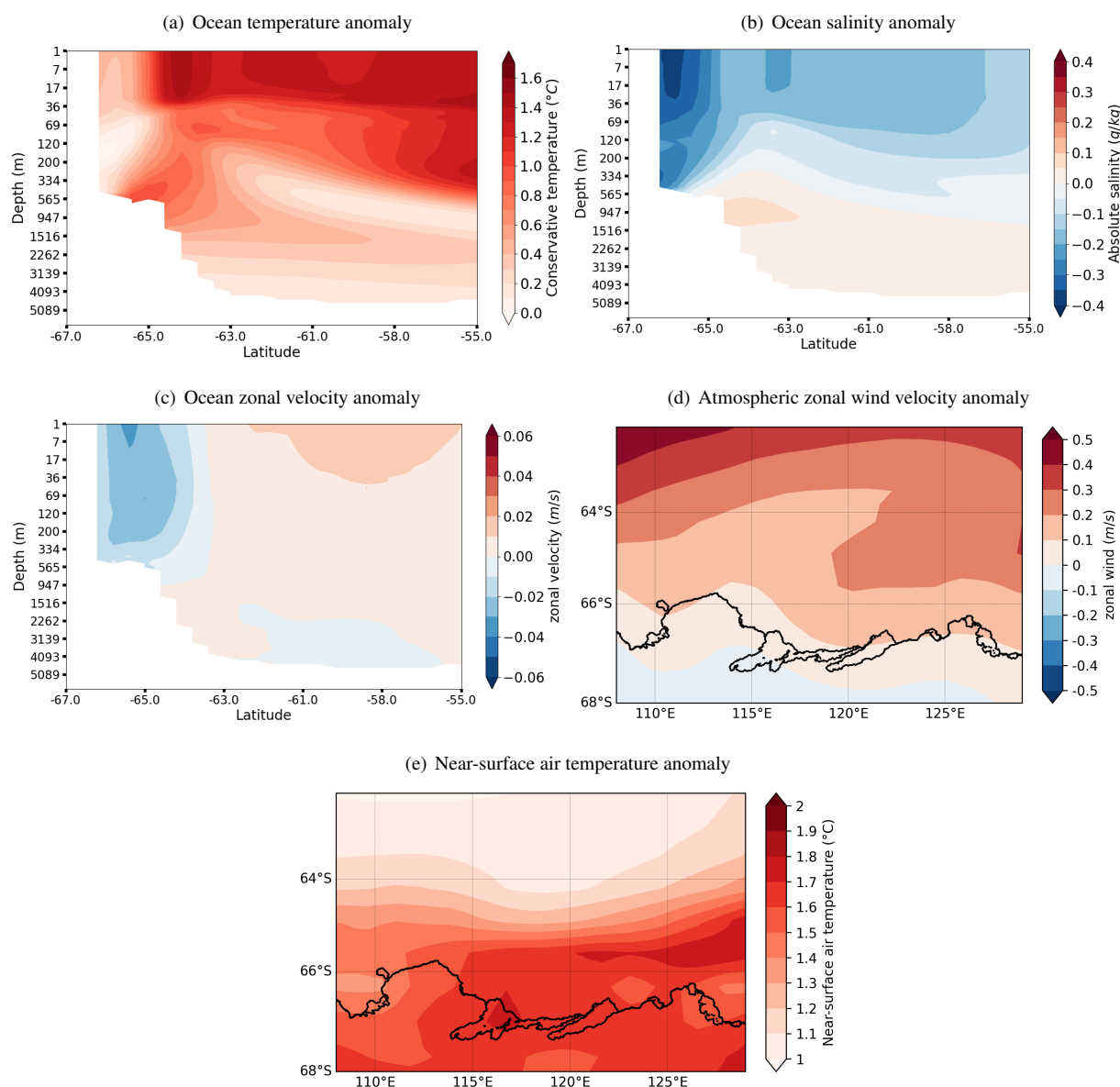140 (Fig 3e), with values larger than $1°$ C and up to $1.8°$ C near the coast.

Figure 3. Annual mean EC-Earth3 anomalies applied at the eastern boundary of the model domain for the conservative temperature (a), absolute salinity (b) and the zonal component of the ocean velocity (c). Annual mean EC–Earth3 anomaly of the wind velocity (10 m) zonal component (d) and the near-surface (2 m) air temperature (e). The anomaly are computed between the 2081-2100 and the 1995-2014 periods.

	Landfast ice	Forcing and lateral boundary conditions
REF	yes	Last decades (ERA5, PARASO, 1995-2014)
WARM	no	REF + anomalies derived from EC–Earth3 climate change projection
nFST	yes	Last decades (ERA5, PARASO, 1995-2014)
nFST_WARM	no	REF + anomalies derived from EC–Earth3 climate change projection

Table 1. Names and descriptions of the simulations used in this study.

3 Results

In this section, we examine the main differences between the results from the REF and WARM simulations. Figures 4a and 4b display the geographical distribution of the fast ice frequency, defined as the percentage of days in a year with a 2-week mean sea ice velocity lower than 0.005 m/s. There is a large retreat of fast ice in WARM compared to REF in front of both the TIS
145 and MUIS. In front of the TIS, the multiyear fast ice cover (frequency above 0.9) in REF is replaced by first year fast ice in WARM. On the other hand, the first year fast ice (frequency between 0.4-0.8) in REF is not at all present in WARM. The same frequency decrease occurs in front of the MUIS, most of the multiyear fast ice in REF becomes first year fast ice in WARM, with a 50% frequency reduction, and the first year fast ice in REF has vanished in WARM. As shown by Figure 4c to 4f, the changes in sea ice concentration over the continental shelf between REF and WARM mostly occur during summer months. In
150 winter, changes are limited to the region off the continental shelf, with a general southward retreat of the ice edge in WARM.
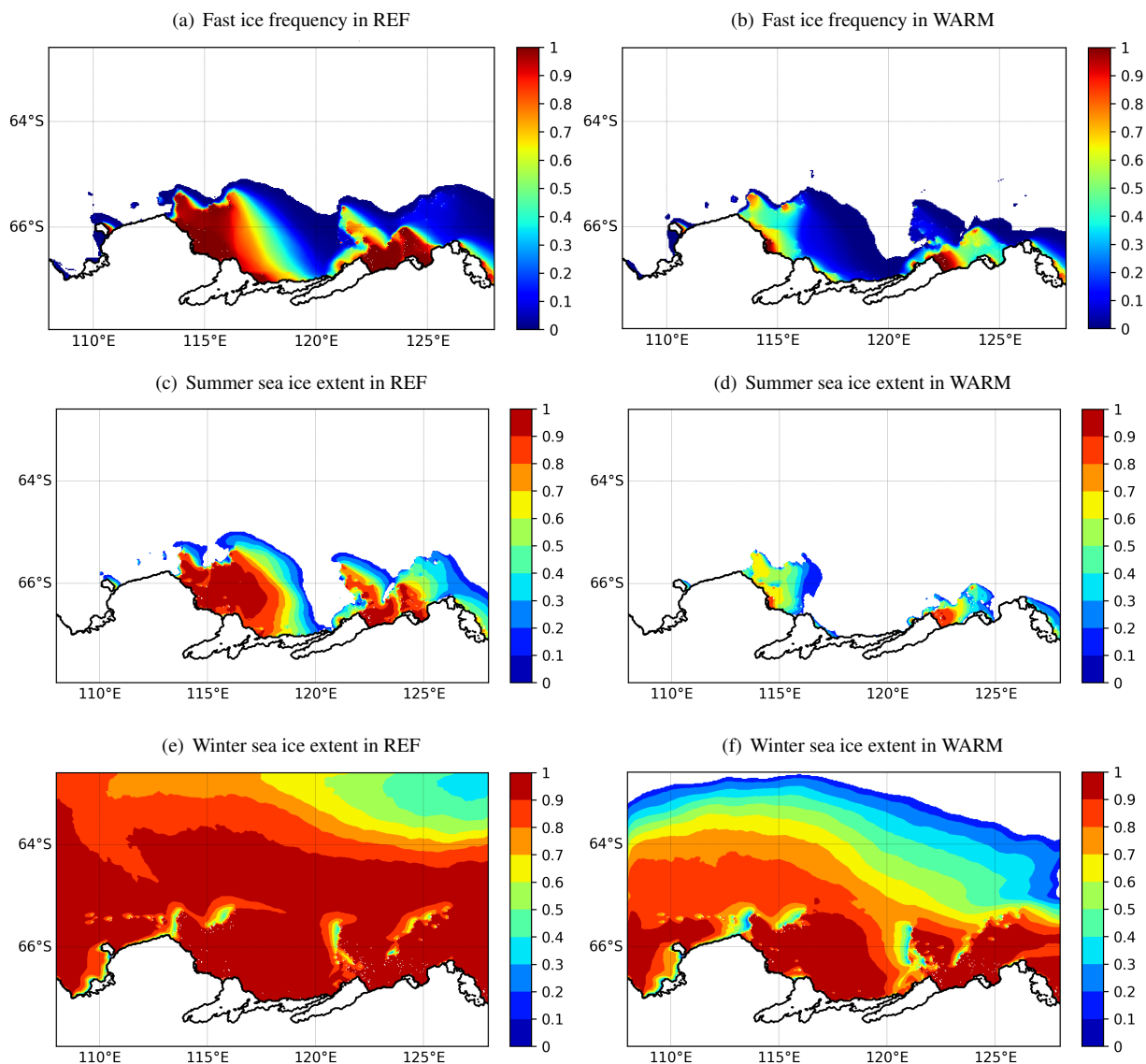
Figure 4. Fast sea ice frequency and sea ice concentration in summer (JFM) and winter (JASO) for the REF (left) and WARM (right) simulations, both averaged over the 20 years of simulations.

Figures 5a and 5b reveal that the ocean circulation experiences major changes between REF and WARM. The ASC, which is barely present in REF, is strongly enhanced in WARM, especially in front of Law Dome and in front of the MUIS (the mean ocean velocity at the ASF is less than 0.1 m/s in REF and is close to 0.15 m/s in WARM). Furthermore, the Totten oceanic gyre in front of the TIS (clockwise oceanic circulation over the shelf) is intensified, especially its western and northern components. This acceleration mainly results from the retreat of fast ice, which acts as a dynamically isolating cover that inhibits the transmission of wind stress to the ocean. Figure 5c shows the annual mean, depth-integrated zonal oceanic volume

transport for both REF and WARM. For each simulation, this mean transport is westwards everywhere (positive value) from the coast until 63°S, with a maximum value near 65°S where the ASC is located (at the shelf break). The eastern transport north of 63°S is associated with the Antarctic Circumpolar Current (ACC). REF and WARM exhibit the same transport pattern, but with a 90% increase in WARM compared to REF.

160

The ASC intensification in WARM is not wind-driven. Indeed, as the pressure gradient across the ASF is enhanced by easterly winds that drive the sea surface height gradient via Ekman drift (Mathiot et al., 2011), an ASC intensification would required stronger easterly winds. Nevertheless, the EC-Earth3 wind velocity anomalies applied to the model in WARM are mostly positive (Fig. 3d), which weakens the easterly winds. This suggests a density-driven origin for the ASC acceleration, as

165 the lateral density gradient across the ASF contributes to establishing the geostrophically balanced, vertically sheared along-slope flows of the ASC (Lockwood et al., 2021). This is coherent with the large density lowering over the continental shelf in WARM compared to REF, which leads to a stronger density gradient across the ASF (Fig. 5d). Since the seawater density is mostly function of salinity in the Southern Ocean (Pellichero et al., 2018), the ASC modification should then be linked to the changes in sea ice production and melt occurring in WARM. This changes, in addition to the EC-Earth3 salinity anomalies

170 prescribed at the eastern boundary of the domain (Fig. 3b), reduce the ocean salinity over the shelf.
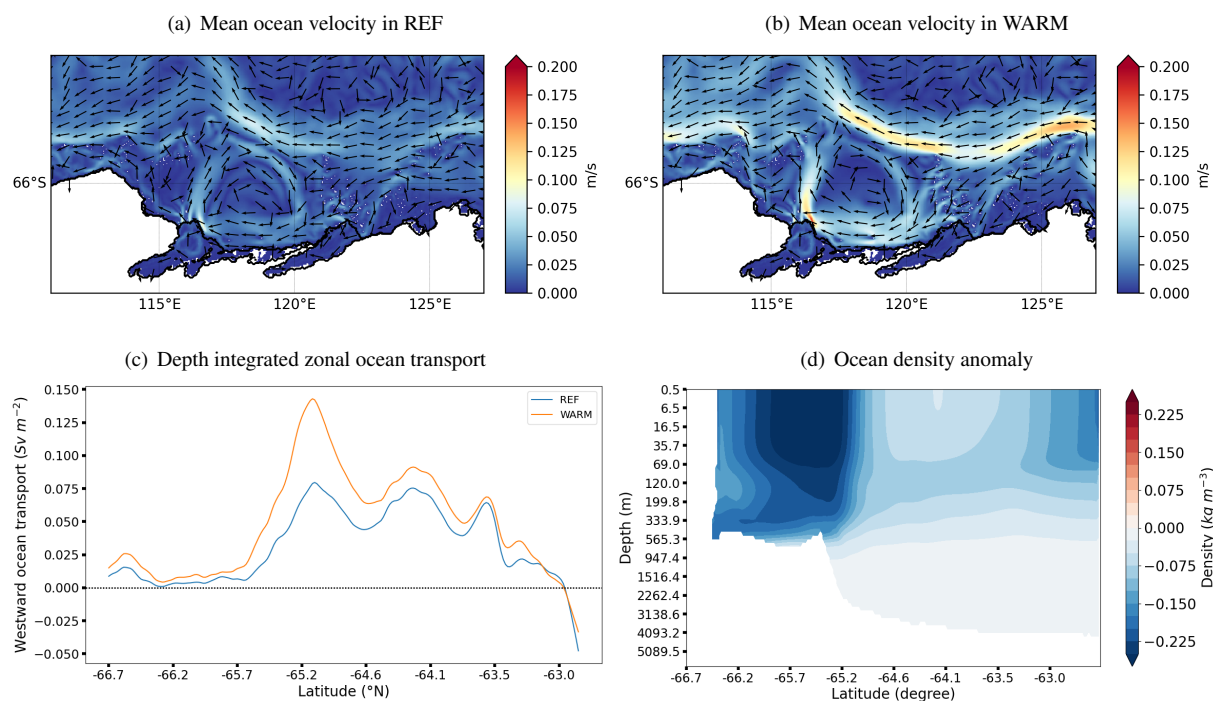

Figure 5. Annual mean, depth-averaged ocean velocity for the REF (a) and WARM (b) simulations, both averaged over the 20 years of simulation. (c) Annual mean, depth-integrated zonal ocean volume transport. (d) Meridional section of the ocean density change between WARM and REF (averaged over 125.3-126.6 E°).

Figure 6 depicts the annual mean ocean temperature differences between WARM and REF (WARM - REF) over the conti-
nental shelf at 200, 300, 400 and 500 m depth. Despite an intensified ASC, which tends to isolate the continental shelf from
the open ocean by reducing the across-shelf exchanges, the ocean temperature over the continental shelf in WARM features
an overall increase. Figure 6a shows warmer water mostly everywhere at 200 m, with a slight warming (from 0.1 to $0.4°$ C)

175 over the shelf and a larger warming (from 0.4 to $1°$ C) in the open ocean. Cooler waters are found on the eastern flank of the
MUIS cavity (from 0 to $-0.2°$ C). The same pattern of temperature difference is noticed at 300 and 400 m (Fig. 6b and 6c),
with a slight cooling next to MUIS and a strong warming in front of TIS, inside the Totten oceanic gyre, where the temperature
increase reaches more than $+1°$ C. Deeper, at 500 m, the temperature difference in front of the MUIS becomes positive (up to
$+0.2°$ C), and the cooling in front of the MUIS is now restricted to the region east of $126°$E (Fig. 6d). The difference of ocean

180 warming between the front of the TIS and the front of MUIS is mostly due to the differences in bathymetry in the two areas.
Indeed, both ice shelves present the same warmer ocean masses at the shelf break but only the deeper bathymetry in front of
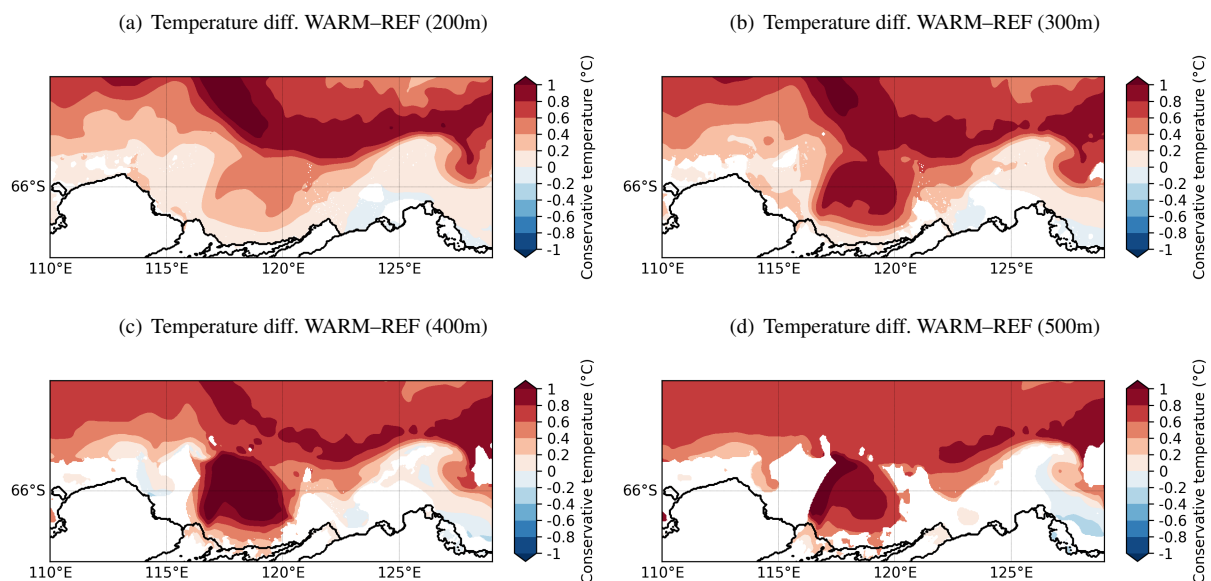the TIS (up to 600 m) allows the warming to reach the TIS cavity.

Figure 6. Annual mean ocean temperature differences between the WARM and REF simulations over the continental shelf at 200, 300, 400
and 500 m depths, all averaged over the 20 years of simulation.

Finally, Figure 7 displays the area-averaged ice shelf basal melt rate for both the TIS and MUIS from REF and WARM.
The TIS experiences a larger (+41%) and more variable (+55%) basal melt rate in WARM, compared to REF. By contrast, the

185 MUIS basal melt rate is almost the same in both simulations (less than 1% increase in WARM), which can be attributed to the
lower ocean warming in front of the MUIS cavity, with less than $+0.2°$ C in front of MUIS compared to more than $+1°$ C in
front of the TIS (see Figure 6).

(a) Area-averaged TIS basal melt rate
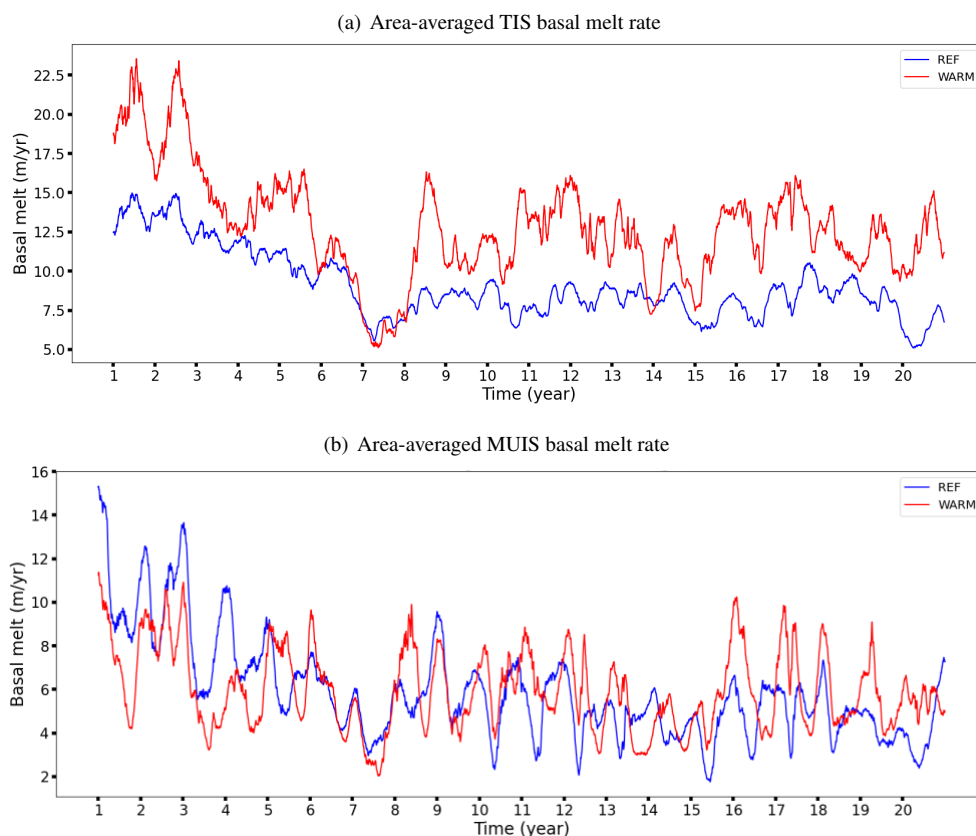

(b) Area-averaged MUIS basal melt rate

Figure 7. Time series of the area-averaged TIS (a) and MUIS (b) basal melt rates from REF (blue) and WARM (red). The time periods are 1995-2014 for REF and 2081-2100 for WARM. The mean TIS basal melt rate is 9.06 ± 4.64 m/yr in REF and 12.8 ± 11.19 m/yr in WARM, while the MUIS basal melt rate is 5.9 ± 5.42 m/yr in REF and 5.95 ± 3.37 m/yr in WARM.

4   Ice shelves melt rate sensitivity to fast ice in a warming climate

In this section, we analyse how the presence of fast ice, implemented through the combination of both a sea ice tensile strength
parameterisation and a representation of grounded icebergs, impacts the changes in ice shelf basal melt rate between the last
decades and the end of the 21st century. The area-averaged TIS and MUIS basal melt rates for both nFST and nFST_WARM
are shown in Figure 8. The TIS has a basal melt rate of 8.09 ± 3.08 m/yr and 12.78 ± 13.34 m/yr in nFST and nFST_WARM,
respectively, whereas the MUIS has a mean basal melt rate of 4.67 ± 2.6 m/yr and 6.44 ± 9.18 m/yr in nFST and nFST_WARM,
respectively.

(a) Area-averaged TIS basal melt rate

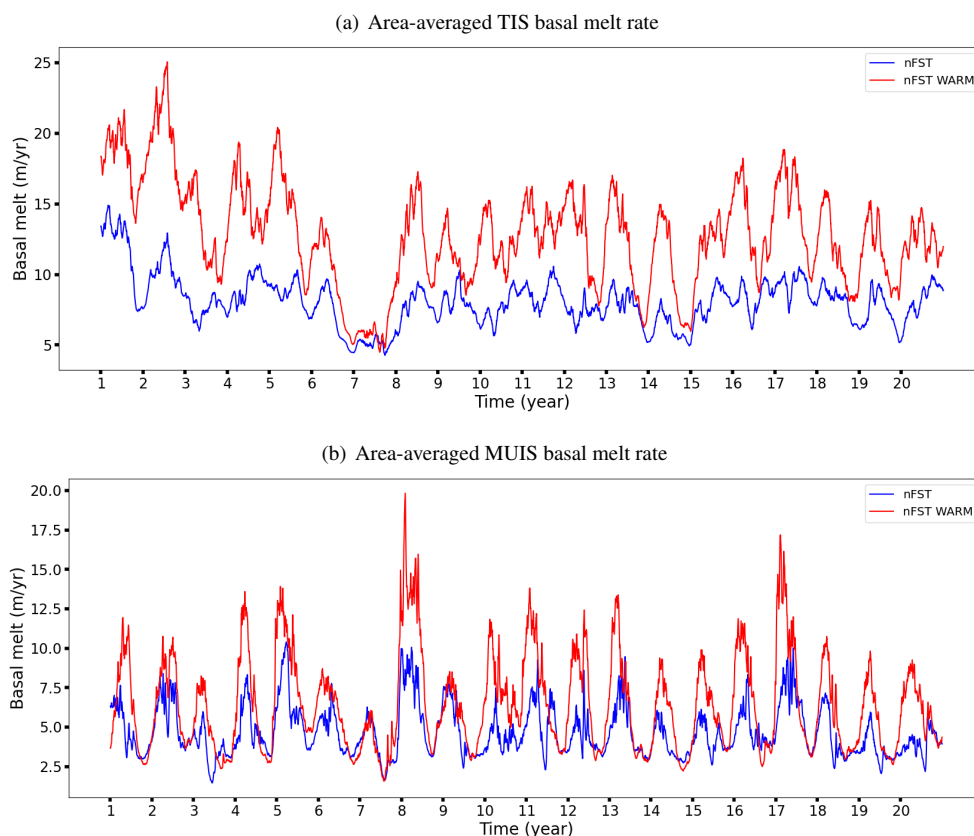(b) Area-averaged MUIS basal melt rate

Figure 8. Time series of the area-averaged TIS (a) and MUIS (b) basal melt rates from nFST (blue) and nFST_WARM (red). The timescale are 1995-2014 and 2018-2100 for the last decades simulations (blue) and the future climate conditions (red), respectively. The time period are 1995-2014 for nFST and 2081-2100 for nFST_WARM. TIS melt rate are 8.09 ± 3.08 m/yr in nFST and 12.78 ± 13.34 m/yr in nFST_WARM. MUIS melt rate are 4.67 ± 2.6 m/yr in nFST and 6.44 ± 9.18 m/yr in nFST_WARM.

195   The mean melt rates at the base of the TIS and MUIS for all simulations are given in Table 2. Without fast ice representation, the increase in basal melt rate for both ice shelves between the two time periods is much larger. This is explained by the strong impact of fast ice on the ice shelf basal melt rate. Indeed, through the displacement of sea ice production zones from coastal to offshore areas, the presence of fast ice induces less sea ice production and more sea ice melt, which increases the ocean stratification in front of the cavities, favors warm water intrusions and increases the basal melt rate in REF compared to nFST.

200   However, as the fast ice disappears under warmer oceanic and atmospheric conditions of the 21st century (Fig. 4a and 4b), this fast ice impact on the basal melt rate is strongly reduced. So, with lower ice shelf melt rates in nFST than in REF but with similar melt rates in WARM and nFST_WARM, the simulations without a fast ice representation are showing a stronger ice shelf melt rate growth between the two periods. In other words, the effect of the reduced extent of fast ice on the ice shelf basal melt rate offsets part of the melt rate increase due to warmer atmospheric and oceanic conditions.

Ice shelves	fast ice	last decades (1995-2014)	end of the 21st century (2081-2100)
Totten	yes	9.06 ± 4.64 m/yr	12.8 ± 11.19 m/yr (+41%)
	no	8.09 ± 3.08 m/yr	12.78 ± 13.34 m/yr (+58%)
Moscow University	yes	5.9 ± 5.42 m/yr	5.95 ± 3.37 m/yr (+1%)
	no	4.67 ± 2.6 m/yr	6.44 ± 9.18 m/yr (+38%)

Table 2. Mean ice shelf basal melt rates for both the last decades and the end of the 21st century and for all simulations.

205   The TIS and MUIS basal melt rates present a different sensitivity to fast ice. This is explained by both the unchanged MUIS basal melt rate in WARM compared to REF, and the higher MUIS basal melt rate in nFST_WARM compared to WARM. Combined, these two effects contribute to a much larger basal melt rate increase between the simulations with and without fast ice for the MUIS than for the TIS (difference of 37% in melt rate increase for MUIS and 17% for TIS). The unchanged MUIS basal melt rate in WARM compared to REF is attributed to the limited effect of the ocean warming over the MUIS cavity,

210   whereas the warmer ocean masses reaches the TIS cavity (Fig. 6d). This is explained by the differences in bathymetry in front of each ice shelf cavity. As described in Van Achter et al. (2022), in REF, the mCDW only reaches the TIS (not the MUIS), which results in an enhanced TIS basal melt rate and a lower MUIS melt rate. In the same way, in WARM, the warmer water masses reach the TIS, but are limited outside of the MUIS cavity, which limits the MUIS basal melt rate changes between REF and WARM. Finally, the higher MUIS basal melt rate in nFST_WARM compared to WARM is attributed to the changes

215   affecting the sea ice in WARM and nFST_WARM. In nFST_WARM, the absence of fast ice allows strong sea ice formation along the coast, with a deep mixed layer depth (mld) in front of the MUIS cavity (Fig. 9c). In contrast, in WARM, the presence of fast ice allows for sea ice formation along the coast but also at the off-shore polynya created on the west side of fast ice patches in front of the MUIS cavity. This combination of sea formation both off-shore and along the coast contributes to broader area of deep mld in front of the MUIS cavity in WARM (Fig. 9d), which decreases the amount of warm water able to cross the

220   continental shelf and to reach the MUIS cavity in WARM compared to nFST_WARM (Fig. 9a and 9b). As a consequence, the MUIS basal melt rate in WARM is lower than in nFST_WARM.
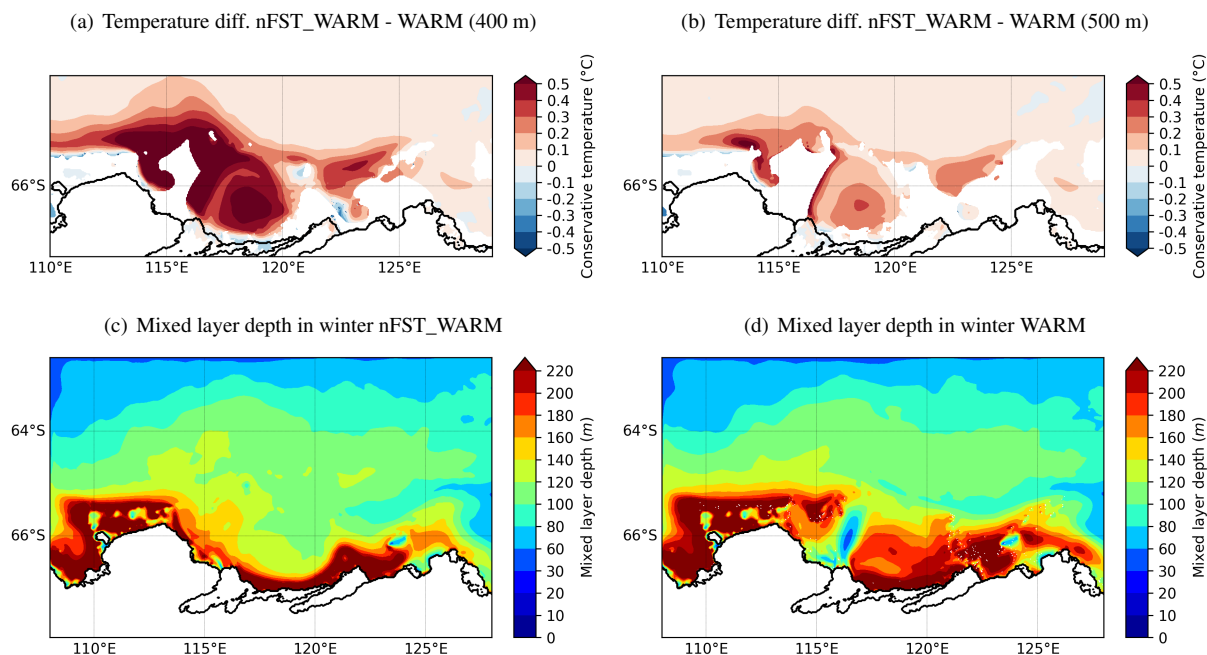
(a) Temperature diff. nFST_WARM - WARM (400 m)   (b) Temperature diff. nFST_WARM - WARM (500 m)

(c) Mixed layer depth in winter nFST_WARM   (d) Mixed layer depth in winter WARM

Figure 9. Annual mean ocean temperature differences between the nFST_WARM and WARM simulations over the continental shelf at 400 (a) and 500 m depths (b). Annual mean mld for nFST_WARM (c) and WARM (d) for the winter months (JASO). Both the temperature anomalies and the mld are averaged over the 20 years simulation.

5 Discussion and conclusions

The first goal of this study was to investigate the ocean–ice shelf interactions under warmer climate conditions in the Totten Glacier region. To do so, we applied climate anomalies, obtained from a SSP4-4.5 climate change projection conducted with
225 EC-Earth3, at the oceanic boundary conditions and atmospheric forcing of a NEMO-LIM high-resolution, regional config- uration, which includes an explicit treatment of ocean–ice shelf interactions and a fast ice representation. Our experiments revealed major changes in ice shelf basal melt rate, sea ice production and ocean circulation between last decades (1995-2014) and the end of the 21st century (2081-2100). The TIS undergoes a drastic basal melt increase (41%), while the MUIS basal melt rate remains almost unchanged (less than 1% increase). Such change in the TIS basal melt rate can be attributed to warmer
230 mCDW (more than $+1°C$) reaching its cavity. On the other hand, these warmer ocean conditions do not affect the MUIS basal melt rate, mainly because of the shallower bathymetry in front of its cavity (less than $+0.2°C$). The warmer atmospheric and oceanic conditions strongly impact the sea ice in the projection run. The fast ice forms less frequently and its coverage is strongly reduced. The sea ice extent is also reduced in both summer and winter. In the ocean, the ASC is largely intensified, with an oceanic zonal volume transport almost twice larger in WARM than in REF. The increase velocity of the ASC seems to
235 be due to the change in density gradient (mostly salinity) across the shelf, triggered by both the sea ice production modification and the changes in ocean lateral boundary conditions.

The second goal of this study was to determine how fast ice influences the increase in ice shelf basal melt rate between the last decades and the end of the 21st century. The representation of fast ice, through the combination of both a sea ice tensile strength parameterisation and the representation of grounded icebergs, has been shown to offset the basal melt rate increase simulated between the last decades and the end of the 21st century. Indeed, for both the TIS and MUIS, the average last decades melt rates are higher with the fast ice representation but are similar by the end of the 21st century, whether or not there is the fast ice representation. The fast ice impact on the melt rate drops as the fast ice extent is reduced due to the warmer oceanic and atmospheric conditions by the end of the 21st century. So, with higher melt rate values for the last decades, but with similar melt rate values by the end of the 21st century, the simulations with fast ice have a lower melt rate growth between the two periods than the simulations without a fast ice representation.

Few other studies investigate the ice shelf melt rate increase between present days and the end of the 21st century in the Totten Glacier area. Moreover, the amount of melt rate increase is strongly linked to the climate change scenario used to force the model. Pelle et al. (2021) simulate a TIS basal melt rate increase of 56% following a high emission scenario, which compares well with our 58% TIS basal melt rate increase (without fast ice). Nevertheless, their simulations present an ASC weakening linked to a freshening at the eastern ocean model boundary, which is the opposite of what we observe in WARM. As recent studies are suggesting both strengthening and weakening of the ASC in the future (Moorman et al., 2020; Pelle et al., 2021), we should aim for better understanding of the ASC changes in East Antarctica.

One of the main limitations of our study lies in the lack of knowledge about the grounded iceberg distribution by the end of the 21st century. In the absence of a day-to-day high-resolution iceberg map, we were forced to use a 2-month icebergs dataset (September–October months of 1997) to prescribe the grounded iceberg location for both the REF (1995-2014) and WARM (2081-2100) simulations. However, a change in the iceberg distribution between REF and WARM might influence the results presented here. Indeed, a modification of the iceberg density in front of the TIS and MUIS cavities could either increase or decrease the fast ice distribution over the continental shelf, and consequently influence how the fast ice change damps the ice shelf basal melt rate under warming conditions. Another limitation in our experimental design, is the use of only one climate change projection. Still about the experimental design, the REF and WARM simulations have the same interannual variability (because WARM is REF with EC–Earth3 anomalies). A WARM simulation with its own interannual variability might change how the TIS and MUIS basal melt rates are enhanced in WARM. Finally, since these results are strongly linked to local processes, it would be interesting to look at the same mechanisms but in other regions of East Antarctica.

Overall, the density-driven ASC acceleration highlights the benefits of high-resolution and accurate continental shelf bathymetric datasets in order to represent lateral density gradients associated with the ASF, and thus to simulate realistically the ASC. This is a major challenge for global climate models, whose relatively coarse resolution prevents such phenomena from being accurately represented (Lockwood et al., 2021). Furthermore, our results underline the worth of a prognostic fast ice representation to simulate future ice shelf melt rate in Antarctica. In contrast to the prescribed fast ice, the prognostic approach enables the fast ice extent to evolve in time. The prognostic representation of fast ice, with time-evolving grounded iceberg locations should be one of the key focus in high-resolution ocean-sea ice modelling in East Antarctica for the years to come.

Author contributions. GVA designed the science plan with TF and HG, ran the simulations, produced the figures, analysed the results and wrote the manuscript based on insights from all co-authors. EMC provided the EC–Earth3 dataset.

Competing interests. The authors declare that they have no known competing financial interests or personal relationships that could have appeared to influence the work reported in this paper.

References

Adcroft, A., Hill, C., and Marshall, J.: Representation of Topography by Shaved Cells in a Height Coordinate Ocean Model, Mon. Weather Rev., 125, 2293 – 2315, https://doi.org/10.1175/1520-0493(1997)125<2293:ROTBSC>2.0.CO;2, 1997.

Aitken, A. R. A., Roberts, J. L., Ommen, T. D. v., Young, D. A., Golledge, N. R., Greenbaum, J. S., Blankenship, D. D., and Siegert, M. J.: Repeated large-scale retreat and advance of Totten Glacier indicated by inland bed erosion, Nature, 533, 385–389, https://doi.org/10.1038/nature17447, 2016.

Bitz, C. M., Holland, M. M., Weaver, A. J., and Eby, M.: Simulating the ice-thickness distribution in a coupled climate model, J. Geophys. Res. Oceans, 106, 2441–2463, https://doi.org/10.1029/1999JC000113, 2001.

Bougeault, P. and Lacarrere, P.: Parameterization of Orography-Induced Turbulence in a Mesobeta–Scale Model, Monthly Weather Review, 117, 1872–1890, https://doi.org/10.1175/1520-0493(1989)117<1872:POOITI>2.0.CO;2, 1989.

Carrère, L., Lyard, F., Cancet, M., Guillot, A., and Roblou, L.: A new global tidal model taking taking advantage of nearly 20 years of altimetry., Proceedings of meeting "20 Years of Altimerty", https://ui.adsabs.harvard.edu/abs/2013ESASP.710E..13C/abstract, 2012.

Dansereau, V., Heimbach, P., and Losch, M.: Simulation of subice shelf melt rates in a general circulation model: Velocity-dependent transfer and the role of friction, J. Geophys. Res. Oceans, 119, 1765–1790, https://doi.org/10.1002/2013JC008846, 2014.

Döscher, R., Acosta, M., Alessandri, A., Anthoni, P., Arneth, A., Arsouze, T., Bergmann, T., Bernadello, R., Bousetta, S., Caron, L.-P., Carver, G., Castrillo, M., Catalano, F., Cvijanovic, I., Davini, P., Dekker, E., Doblas-Reyes, F. J., Docquier, D., Echevarria, P., Fladrich, U., Fuentes-Franco, R., Gröger, M., v. Hardenberg, J., Hieronymus, J., Karami, M. P., Keskinen, J.-P., Koenigk, T., Makkonen, R., Massonnet, F., Ménégoz, M., Miller, P. A., Moreno-Chamarro, E., Nieradzik, L., van Noije, T., Nolan, P., O'Donnell, D., Ollinaho, P., van den Oord, G., Ortega, P., Prims, O. T., Ramos, A., Reerink, T., Rousset, C., Ruprich-Robert, Y., Le Sager, P., Schmith, T., Schrödner, R., Serva, F., Sicardi, V., Sloth Madsen, M., Smith, B., Tian, T., Tourigny, E., Uotila, P., Vancoppenolle, M., Wang, S., Wårlind, D., Willén, U., Wyser, K., Yang, S., Yepes-Arbós, X., and Zhang, Q.: The EC-Earth3 Earth System Model for the Climate Model Intercomparison Project 6, Geoscientific Model Development Discussions, 2021, 1–90, https://doi.org/10.5194/gmd-2020-446, 2021.

Engedahl, H.: Use of the flow relaxation scheme in a three-dimensional baroclinic ocean model with realistic topography, Tellus A: Dynamic Meteorology and Oceanography, 47, 365–382, https://doi.org/10.3402/tellusa.v47i3.11523, 1995.

Eyring, V., Bony, S., Meehl, G. A., Senior, C. A., Stevens, B., Stouffer, R. J., and Taylor, K. E.: Overview of the Coupled Model Intercomparison Project Phase 6 (CMIP6) experimental design and organization, Geoscientific Model Development, 9, 1937–1958, https://doi.org/10.5194/gmd-9-1937-2016, 2016.

Flather, R. A.: A Storm Surge Prediction Model for the Northern Bay of Bengal with Application to the Cyclone Disaster in April 1991, J. Phys. Oceanogr., 24, 172–190, https://doi.org/10.1175/1520-0485(1994)024<0172:ASSPMF>2.0.CO;2, 1994.

Fraser, A. D., Massom, R. A., Michael, K. J., Galton-Fenzi, B. K., and Lieser, J. L.: East Antarctic Landfast Sea Ice Distribution and Variability, 2000–08, J. Climate, 25, 1137–1156, https://doi.org/10.1175/JCLI-D-10-05032.1, 2012.

Fraser, A. D., Massom, R. A., Ohshima, K. I., Willmes, S., Kappes, P. J., Cartwright, J., and Porter-Smith, R.: High-resolution mapping of circum-Antarctic landfast sea ice distribution, 2000–2018, Earth Syst. Sci. Data, 12, 2987–2999, https://doi.org/10.5194/essd-12-2987-2020, 2020.

Gaspar, P., Grégoris, Y., and Lefevre, J.-M.: A simple eddy kinetic energy model for simulations of the oceanic vertical mixing: Tests at station Papa and long-term upper ocean study site, J. Geophys. Res. Oceans, 95, 16 179–16 193, https://doi.org/10.1029/JC095iC09p16179, 1990.

Greenbaum, J. S., Blankenship, D. D., Young, D. A., Richter, T. G., Roberts, J. L., Aitken, A. R. A., Legresy, B., Schroeder, D. M., Warner, R. C., van Ommen, T. D., and Siegert, M. J.: Ocean access to a cavity beneath Totten Glacier in East Antarctica, Nature Geoscience, 8, 294–298, https://doi.org/10.1038/ngeo2388, 2015.

320 Greene, C. A., Young, D. A., Gwyther, D. E., Galton-Fenzi, B. K., and Blankenship, D. D.: Seasonal dynamics of Totten Ice Shelf controlled by sea ice buttressing, The Cryosphere, 12, 2869 – 2882, https://doi.org/10.5194/tc-12-2869-2018, 2018.

Hellmer, H. H., Kauker, F., Timmermann, R., Determann, J., and Rae, J.: Twenty-first-century warming of a large Antarctic ice-shelf cavity by a redirected coastal current, Nature, 485, 225–228, https://doi.org/10.1038/nature11064, 2012.

Hersbach, H., Bell, B., Berrisford, P., Hirahara, S., Horányi, A., Muñoz-Sabater, J., Nicolas, J., Peubey, C., Radu, R., Schepers, D., Simmons, 325 A., Soci, C., Abdalla, S., Abellan, X., Balsamo, G., Bechtold, P., Biavati, G., Bidlot, J., Bonavita, M., De Chiara, G., Dahlgren, P., Dee, D., Diamantakis, M., Dragani, R., Flemming, J., Forbes, R., Fuentes, M., Geer, A., Haimberger, L., Healy, S., Hogan, R. J., Hólm, E., Janisková, M., Keeley, S., Laloyaux, P., Lopez, P., Lupu, C., Radnoti, G., de Rosnay, P., Rozum, I., Vamborg, F., Villaume, S., and Thépaut, J.-N.: The ERA5 global reanalysis, Q. J. R. Meteorol. Soc., 146, 1999–2049, https://doi.org/10.1002/qj.3803, 2020.

Huot, P.-V., Fichefet, T., Jourdain, N. C., Mathiot, P., Rousset, C., Kittel, C., and Fettweis, X.: Influence of ocean tides and ice 330 shelves on ocean–ice interactions and dense shelf water formation in the D'Urville Sea, Antarctica, Ocean Model., 162, 101 794, https://doi.org/https://doi.org/10.1016/j.ocemod.2021.101794, 2021.

IOC: The International thermodynamic equation of seawater: calculation and use of thermodynamic properties, Tech. rep., UNESCO, https: //unesdoc.unesco.org/ark:/48223/pf0000188170, intergovernmental Oceanographic Commission, 2010.

Jacobs, S. S.: On the nature and significance of the Antarctic Slope Front, Marine Chemistry, 35, 9–24, 335 https://doi.org/https://doi.org/10.1016/S0304-4203(09)90005-6, biochemistry and circulation of water masses in the Southern Ocean, 1991.

Jenkins, A.: A one-dimensional model of ice shelf-ocean interaction, J. Geophys. Res., 96, 20 671–20 677, https://doi.org/10.1029/91JC01842, 1991.

Jezek, K. C., Curlander, J. C., Carsey, F., Wales, C., and Barry, R. G.: RAMP AMM-1 SAR Image Mosaic of Antarctica, Version 340 2. [Indicate subset used], Boulder, Colorado USA. NASA National Snow and Ice Data Center Distributed Active Archive Center, https://doi.org/10.5067/8AF4ZRPULS4H, 2013.

Jourdain, N. C., Mathiot, P., Merino, N., Durand, G., Le Sommer, J., Spence, P., Dutrieux, P., and Madec, G.: Ocean circulation and sea-ice thinning induced by melting ice shelves in the Amundsen Sea, J. Geophys. Res. Oceans, 122, 2550–2573, https://doi.org/10.1002/2016JC012509, 2017.

345 Jourdain, N. C., Molines, J.-M, Le Sommer, J., Mathiot, P., Chanut, J., de Lavergne, C., and Madec, G.: Simulating or prescribing the influence of tides on the Amundsen Sea ice shelves, Ocean Model., 133, 44 – 55, https://doi.org/10.1016/j.ocemod.2018.11.001, 2019.

Khazendar, A., Schodlok, M., Fenty, I., Ligtenberg, S., Rignot, E., and van den Broeke, M.: Observed thinning of Totten Glacier is linked to coastal polynya variability, Nat. Commun., 4, https://doi.org/10.1038/ncomms3857, 2013.

Large, W. and Yeager, S.: Diurnal to decadal global forcing for ocean and sea-ice models: the data sets and flux climatologie, UCAR, 350 https://doi.org/10.5065/D6KK98Q6, 2004.

Lemieux, J.-F., Dupont, F., Blain, P., Roy, F., Smith, G. C., and Flato, G. M.: Improving the simulation of landfast ice by combining tensile strength and a parameterization for grounded ridges, J. Geophys. Res. Oceans, 121, 7354–7368, https://doi.org/10.1002/2016JC012006, 2016.

Lockwood, J. W., Dufour, C. O., Griffies, S. M., and Winton, M.: On the Role of the Antarctic Slope Front on the Occurrence of the Weddell
355   Sea Polynya under Climate Change, Journal of Climate, 34, 2529 – 2548, https://doi.org/10.1175/JCLI-D-20-0069.1, 2021.

Losch, M.: Modeling ice shelf cavities in a z coordinate ocean general circulation model, J. Geophys. Res. Oceans, 113,
       https://doi.org/10.1029/2007JC004368, 2008.

Madec, G.: NEMO ocean engine, Note du Pole de modelisation, Institut Pierre-Simon Laplace (IPSL), France, No 27, ISSN No 1288-1619,
       2008.

360   Madec, G., Delecluse, P., Imbard, M., and Levy, C.: 1 Ocean General Circulation Model reference manual, 1998.

Maraldi, C., Chanut, J., Levier, B., Ayoub, N., De Mey, P., Reffray, G., Lyard, F., Cailleau, S., Drévillon, M., Fanjul, E. A., Sotillo, M. G.,
       Marsaleix, P., the Mercator Research, and Team, D.: NEMO on the shelf: assessment of the Iberiandash;Biscayndash;Ireland configuration,
       Ocean Sci., 9, 745–771, https://doi.org/10.5194/os-9-745-2013, 2013.

Massom, R. A., Hill, K. L., Lytle, V. I., Worby, A. P., Paget, M., and Allison, I.: Effects of regional fast-ice and iceberg distributions on
365   the behaviour of the Mertz Glacier polynya, East Antarctica, Ann. Glaciol., 33, 391–398, https://doi.org/10.3189/172756401781818518,
       2001.

Massonnet, F., Goosse, H., Fichefet, T., and Counillon, F.: Calibration of sea ice dynamic parameters in an ocean-sea ice model using an
       ensemble Kalman filter, Journal of Geophysical Research: Oceans, 119, 4168–4184, https://doi.org/10.1002/2013JC009705, 2014.

Mathiot, P., Goosse, H., Fichefet, T., Barnier, B., and Gallée, H.: Modelling the seasonal variability of the Antarctic Slope Current, Ocean
370   Science, 7, 455–470, https://doi.org/10.5194/os-7-455-2011, 2011.

Mathiot, P., Jenkins, A., Harris, C., and Madec, G.: Explicit representation and parametrised impacts of under ice shelf seas in the z^*
       coordinate ocean model NEMO 3.6, Geosci. Model Dev., 10, 2849–2874, https://doi.org/10.5194/gmd-10-2849-2017, 2017.

Moorman, R., Morrison, A. K., and Hogg, A. M.: Thermal Responses to Antarctic Ice Shelf Melt in an Eddy-Rich Global Ocean–Sea Ice
       Model, Journal of Climate, 33, 6599 – 6620, https://doi.org/10.1175/JCLI-D-19-0846.1, 2020.

375   Morlighem, M., Rignot, E., Binder, T., Blankenship, D., Drews, R., Eagles, G., Eisen, O., Forsberg, R., Fretwell, P., Goel, V., Greenbaum, J.,
       Gudmundsson, G., Guo, J., Helm, V., Hofstede, C., Howat, I., Humbert, A., Jokat, W., and Young, D.: Deep glacial troughs and stabilizing
       ridges unveiled beneath the margins of the Antarctic ice sheet, Nat. Geosci., 13, 1–6, https://doi.org/10.1038/s41561-019-0510-8, 2020.

Nakayama, Y., Greene, C. A., Paolo, F. S., Mensah, V., Zhang, H., Kashiwase, H., Simizu, D., Greenbaum, J. S., Blankenship, D. D., Abe-
       Ouchi, A., and Aoki, S.: Antarctic Slope Current Modulates Ocean Heat Intrusions Towards Totten Glacier, Geophysical Research Letters,
380   48, e2021GL094 149, https://doi.org/10.1029/2021GL094149, 2021.

Naughten, K. A., Meissner, K. J., Galton-Fenzi, B. K., England, M. H., Timmermann, R., and Hellmer, H. H.: Future Projections of Antarctic
       Ice Shelf Melting Based on CMIP5 Scenarios, Journal of Climate, 31, 5243 – 5261, https://doi.org/10.1175/JCLI-D-17-0854.1, 2018.

Paolo, F. S., Fricker, H. A., and Padman, L.: Volume loss from Antarctic ice shelves is accelerating, Science, 348, 327–331,
       https://doi.org/10.1126/science.aaa0940, 2015.

385   Pelle, T., Morlighem, M., Nakayama, Y., and Seroussi, H.: Widespread Grounding Line Retreat of Totten Glacier, East Antarctica, Over the
       21st Century, Geophys. Res. Lett., 48, e2021GL093 213, https://doi.org/10.1029/2021GL093213, 2021.

Pelletier, C., Fichefet, T., Goosse, H., Haubner, K., Helsen, S., Huot, P.-V., Kittel, C., Klein, F., Le clec'h, S., van Lipzig, N. P. M., Marchi, S.,
       Massonnet, F., Mathiot, P., Moravveji, E., Moreno-Chamarro, E., Ortega, P., Pattyn, F., Souverijns, N., Van Achter, G., Vanden Broucke, S.,
       Vanhulle, A., Verfaillie, D., and Zipf, L.: PARASO, a circum-Antarctic fully-coupled ice-sheet - ocean - sea-ice - atmosphere - land model
390   involving f.ETISh1.7, NEMO3.6, LIM3.6, COSMO5.0 and CLM4.5, Geosci. Model Dev., 15, 553–594, https://doi.org/10.5194/gmd-
       2021-315, 2022.

Pellichero, V., Sallée, J.-B., Chapman, C. C., and Downes, S. M.: The southern ocean meridional overturning in the sea-ice sector is driven by freshwater fluxes, Nat. Commun., 9, https://doi.org/10.1038/s41467-018-04101-2, 2018.

Rignot, E., Jacobs, S., Mouginot, J., and Scheuchl, B.: Ice-Shelf Melting Around Antarctica, Science, 341, 266–270, https://doi.org/10.1126/science.1235798, 2013.

Rintoul, S. R., Silvano, A., Pena-Molino, B., van Wijk, E., Rosenberg, M., Greenbaum, J. S., and Blankenship, D. D.: Ocean heat drives rapid basal melt of the Totten Ice Shelf, Sci. Adv., 2, https://doi.org/10.1126/sciadv.1601610, 2016.

Roberts, J. L., Warner, R. C., Young, D., Wright, A., van Ommen, T. D., Blankenship, D. D., Siegert, M., Young, N. W., Tabacco, I. E., Forieri, A., Passerini, A., Zirizzotti, A., and Frezzotti, M.: Refined broad-scale sub-glacial morphology of Aurora Subglacial Basin, East Antarctica derived by an ice-dynamics-based interpolation scheme, The Cryosphere, 5, 551–560, https://doi.org/10.5194/tc-5-551-2011, 2011.

Roquet, F., Williams, G., Hindell, M. A., Harcourt, R., McMahon, C., Guinet, C., Charrassin, J.-B., Reverdin, G., Boehme, L., Lovell, P., and Fedak, M.: A Southern Indian Ocean database of hydrographic profiles obtained with instrumented elephant seals, Scientific Data, 1, https://doi.org/10.1038/sdata.2014.28, 2014.

Rousset, C., Vancoppenolle, M., Madec, G., Fichefet, T., Flavoni, S., Barthélemy, A., Benshila, R., Chanut, J., Levy, C., Masson, S., and Vivier, F.: The Louvain-La-Neuve sea ice model LIM3.6: global and regional capabilities, Geosci. Model Dev., 8, 2991–3005, https://doi.org/10.5194/gmd-8-2991-2015, 2015.

Stewart, A. L., Klocker, A., and Menemenlis, D.: Circum-Antarctic Shoreward Heat Transport Derived From an Eddy- and Tide-Resolving Simulation, Geophysical Research Letters, 45, 834–845, https://doi.org/10.1002/2017GL075677, 2018.

Thompson, A. F., Stewart, A. L., Spence, P., and Heywood, K. J.: The Antarctic Slope Current in a Changing Climate, Reviews of Geophysics, 56, 741–770, https://doi.org/10.1029/2018RG000624, 2018.

Timmermann, R. and Goeller, S.: Response to Filchner–Ronne Ice Shelf cavity warming in a coupled ocean–ice sheet model – Part 1: The ocean perspective, Ocean Science, 13, 765–776, https://doi.org/10.5194/os-13-765-2017, 2017.

Van Achter, G., Fichefet, T., Goosse, H., Pelletier, C., Sterlin, J., Huot, P.-V., Lemieux, J.-F., Fraser, A. D., Haubner, K., and Porter-Smith, R.: Modelling landfast sea ice and its influence on ocean–ice interactions in the area of the Totten Glacier, East Antarctica, Ocean Model., 169, 101 920, https://doi.org/10.1016/j.ocemod.2021.101920, 2022.

Vancoppenolle, M., Fichefet, T., Goosse, H., Bouillon, S., Madec, G., and Maqueda, M.: Simulating the mass balance and salinity of Arctic and Antarctic sea ice. 1. Model description and validation, Ocean Model., 27, 33 – 53, https://doi.org/10.1016/j.ocemod.2008.10.005, 2009.

Whitworth, T., Orsi, A. H., Kim, S.-J., Nowlin Jr., W. D., and Locarnini, R. A.: Water Masses and Mixing Near the Antarctic Slope Front, pp. 1–27, American Geophysical Union (AGU), https://doi.org/10.1029/AR075p0001, 1985.

WMO: WMO sea-ice nomenclature. Terminology, codes and illustrated glossary, Tech. Rep., 259, 1970.